

# Pulse Wave Modeling using Bio-Impedance Simulation Platform based on a 3D Time-Varying Circuit Model

Bassem Ibrahim, *Student Member, IEEE*, Drew A. Hall, *Senior Member, IEEE*  
and Roozbeh Jafari, *Senior Member, IEEE*

**Abstract**—Cardiovascular disease (CVD) threatens the lives of many and affects their productivity. CVD is diagnosed through hemodynamic parameters that vary significantly throughout the day. Wearable sensors can enable continuous monitoring of hemodynamic parameters to improve the diagnosis and management of CVD. Bio-Impedance (Bio-Z) is an effective non-invasive sensor for arterial pulse wave monitoring based on blood volume changes in the artery due to the deep penetration of its current signal inside the tissue. However, the measured data are significantly affected by the placement of electrodes relative to the artery and the electrode configuration. In this work, we created a Bio-Z simulation platform that models the tissue, arterial pulse wave, and Bio-Z sensing configuration using a 3D circuit model based on a time-varying impedance grid. A new method is proposed to accurately simulate the different tissue types such as blood, fat, muscles, and bones in a 3D circuit model in addition to the pulsatile activity of the arteries through a variable impedance model. This circuit model is simulated in SPICE and can be used to guide design decisions (*i.e.* electrode placement relative to the artery and electrode configuration) to optimize the monitoring of pulse wave prior to experimentation. We present extensive simulations of the arterial pulse waveform for different sensor locations, electrode sizes, current injection frequencies, and artery depths. The simulations are validated by experimental Bio-Z measurements. This model will enable researchers and designers to create time-varying blood flow models and rapidly test the effectiveness of the sensing methods and algorithms without the need for extensive experimentation.

**Index Terms**— Bio-impedance, simulation, 3D tissue model, pulse wave

## I. INTRODUCTION

CARDIOVASCULAR disease (CVD) is the leading cause of death worldwide accounting for 17.8 million deaths

Manuscript received XXXXXXXXXXXX; revised YYYYYYYYYY; accepted ZZZZZZZZZZ. This paper was approved by Associate Editor ABCD XYZAASDDDFSD. This work was supported in part by the National Institutes of Health, under Grants 1R01EB028106-01 and 1R01HL151240-01A1. (*Corresponding author: Bassem Ibrahim*).

B. Ibrahim is with the Department of Electrical and Computer Engineering, Texas A&M University, College Station, TX 77843 USA (e-mail: [bassem@tamu.edu](mailto:bassem@tamu.edu)).

D. Hall is with the Department of Electrical and Computer Engineering, University of California, San Diego, La Jolla, CA 92093 USA. (e-mail: [drewhall@ucsd.edu](mailto:drewhall@ucsd.edu)).

R. Jafari is with the Departments of Biomedical, Computer Science and Engineering, and Electrical Engineering, Texas A&M University, College Station, TX 77843 USA (e-mail: [rjafari@tamu.edu](mailto:rjafari@tamu.edu)).

Color versions of one or more figures in this paper are available online at <http://ieeexplore.ieee.org>.

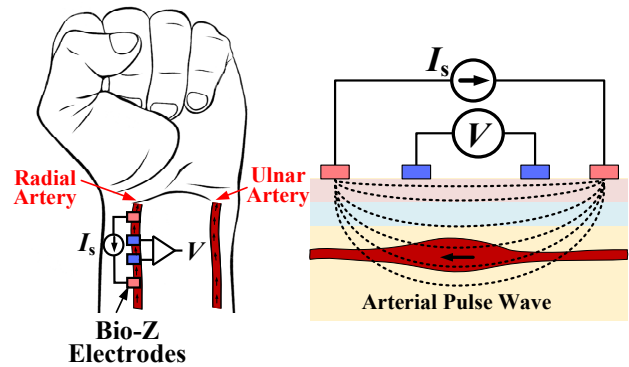


Fig. 1. Overview of Bio-Z sensing of arterial pulse wave from the wrist arteries.

(23.4%) in 2017 [1, 2]. The global cost of CVD due to healthcare and loss in productivity is expected to increase continuously to reach >1 trillion USD in 2030 [3]. Diagnosis and management of CVD depend heavily on the monitoring of hemodynamic parameters such as blood pressure (BP), pulse transit time (PTT), vascular compliance, and cardiac output. These parameters vary considerably throughout the day and with activity. Continuous hemodynamic monitoring can improve the diagnosis and management of CVD. For example, high blood pressure at night-time is associated with a higher risk of a CVD event [4]. However, the conventional method for blood pressure monitoring with obtrusive, bulky cuffs is not suitable for continuous monitoring. Thus, there is a strong need for new non-invasive, continuous hemodynamic monitoring methods that can be integrated into wearable devices. Arterial pulse wave has been used extensively for continuous measurement of hemodynamic parameters through monitoring the pulsation of blood inside the arteries [5, 6]. PTT, which is the time delay of the pulse wave traveling between two points along an artery, can be used for BP estimation through a cuffless method with non-invasive and comfortable sensors [7, 8].

Bio-Impedance (Bio-Z) is a non-invasive bio-electrical sensor that can measure effectively pulse wave in the arteries through the deep penetration of electrical signals in the tissue. Bio-Z probes the fluid inside the body by injecting a small AC current and measuring the resulting voltage through separate pairs of electrodes attached to the skin (*i.e.* 4-probe Kelvin sensing), as shown in Fig. 1 [9-11]. When the Bio-Z sensor is

placed close to the artery, it can measure arterial pulse wave from the blood volume changes. Previous work showed that PTT can be measured by a small form-factor Bio-Z sensor from the delay between two voltage signals measured from two pairs of electrodes over a short distance along the artery, as shown in Fig. 2(a) [12, 13]. In addition, Bio-Z signals were validated to estimate BP from wrist-worn sensors based on PTT and other features extracted from the morphology of the arterial pulse wave measured from the wrist arteries [14, 15]. One of the main challenges of arterial pulse sensing using Bio-Z is the lack of efficient simulation tools that help one to understand the electrical response of the tissue and blood flow for the applied current signal stimulus versus the different sensing parameters, such as the sensing location relative to the artery, electrode configuration, current injection frequency, and artery's depth.

In this paper, we propose a 3D circuit model for the tissue and blood pulsation based on a time-varying 3D impedance grid to model dynamic activities inside the body such as arterial pulse wave, as shown in Fig. 2(b). The tissue is modeled using a 3D grid of small, interconnected, time-varying impedance elements (voxels). Each voxel consists of the equivalent circuit of cells that represent different tissue types. The blood flow inside arteries is modeled by a time-varying voxel impedance that represents the artery to simulate blood volume changes and pulse wave propagation. A parameterized SPICE model is used to describe the geometry and conductivity of the modeled tissue, diameter, depth, and location of the arteries, and the location and spacing of the electrodes on the skin. The 3D aspect of the proposed model provides more accurate modeling of the tissue and the sensing signals compared to 2D models. The injected current signal flows in 3D space inside the tissue, therefore the 3D model provides an accurate distribution of current and potential in space compared to 2D models that neglect fringe currents that flow in the third dimension. In addition, the proposed 3D model provides complex sensing configurations for the pulse wave that are not possible with 2D models such as modeling the effect of moving the Bio-Z electrodes orthogonal to the artery's direction on the sensed pulse signal.

The general blood flow model can be divided into two parts as shown in Fig. 2(c): the first part is the mechanical model that generates the blood volume changes due to blood pressure changes taking into account the arterial stiffness and blood flow dynamics, while the second part is the electrical model that converts the blood volume changes into electrical signals by the Bio-Z sensor. In this work, we focus on the second part of the electrical model by considering the electrical properties of the tissue and blood volume changes as circuit models. We used a simple linear mechanical model for the blood flow and blood volume changes to show the performance of our electrical model, however, our modeling approach is flexible and can be augmented by any mechanical model for the blood volume changes for a more complex blood flow model.

To demonstrate the utility and validity of the model, we present the simulation of the arterial pulse wave and PTT monitoring from the wrist arteries for different sensing locations and parameters validated by extensive experimental

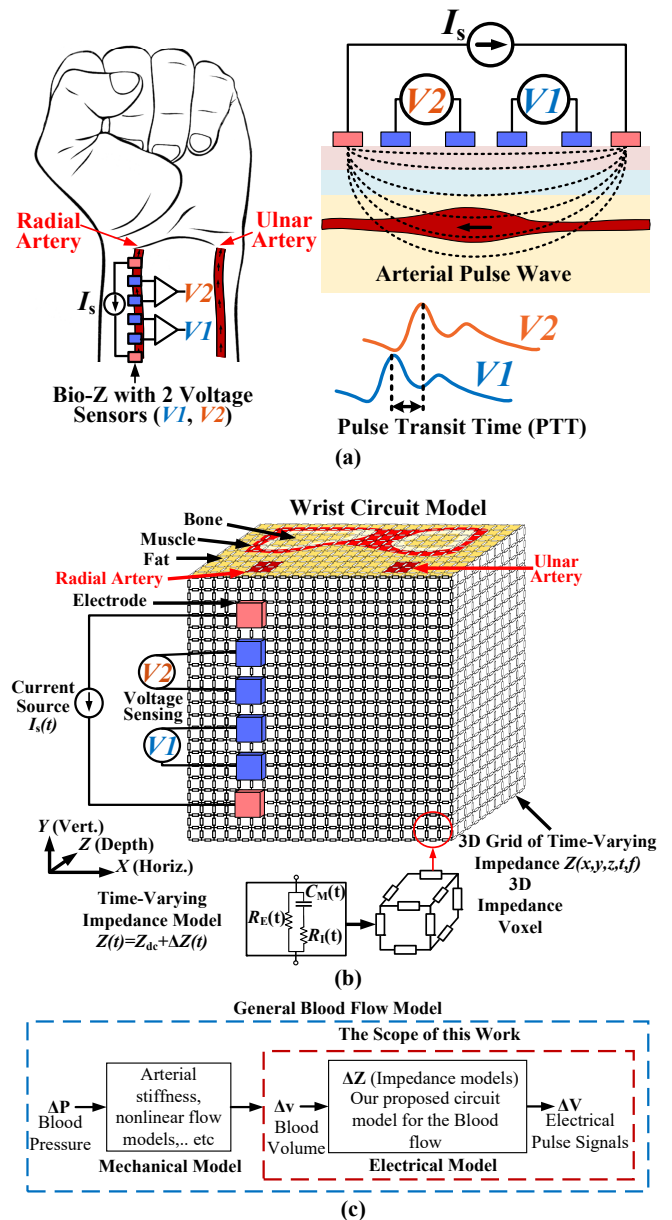


Fig. 2. (a) Bio-Z sensing for PTT from the wrist, (b) Overview of the proposed wrist circuit model for Bio-Z simulation platform based on a 3D time-varying impedance grid that models arterial pulse wave and PTT, (c) the scope of this work focuses on the proposed electrical model of blood flow which can be augmented by any mechanical model to provide complex blood flow model.

characterization. The source code of the proposed model with examples are available online to help designers and researchers to simulate different parts of the body with different blood flow properties and sensing configuration to understand design tradeoffs [16]. This simulation framework helps in understanding the electrical response of the tissue and blood flow, and the optimization of circuits and algorithms of arterial pulse sensing without the need for extensive experimentation. Our previous work [17] is extended in this manuscript by improving the tissue circuit model through presenting a complete 3D circuit model of the wrist similar to the anatomy of the wrist by modeling the impedance and electrical properties

of the different tissue types of the wrist such as fat, muscle, and bone in addition to the skin-electrode impedance. Furthermore, the blood flow model is extended to model the arterial pulse wave in both radial and ulnar arteries of the wrist. We include a new simulation for the whole wrist model validated by experimental data to show the effect of changing the sensing location and the current injection frequency on the pulse signal.

The rest of the paper is organized as follows. Background material is discussed in Section II, followed by the description of the methods in Section III. Then, we present simulation and experimental results in Section IV. Concluding remarks are presented in Section V.

## II. BACKGROUND

Simple cardiac parameters like heart rate can be measured from the pulsation of surface blood vessels such as capillaries and veins; however, complex cardiac parameters such as BP and PTT require accurate measurement of the arterial pulse wave generated from the pulsation of arteries – the deep, main blood vessels that carry the oxygenated blood from the heart to the rest of the body. Bio-Z is superior at detecting arterial pulse wave compared to other modalities such as optical sensors like photoplethysmograph (PPG) for the following reasons: 1) Optical sensors only capture blood volume changes near the skin surface (*i.e.* from capillaries) because light has limited penetration into the tissue (up to 3 mm) [18, 19]. On the other hand, since Bio-Z relies on a current signal, it can reach deeper tissue [20]. Thus, the Bio-Z signal can reach deep arterial sites to provide more accurate monitoring of arterial blood volume changes. 2) Bio-Z is not affected by ambient light and skin tone, unlike PPG. 3) Bio-Z has a wider application space such as respiration and hydration measurements, further increasing its utility [20, 21].

One of the challenges in arterial pulse sensing with Bio-Z is the variation of the pulse morphology and features with the sensing parameters. As shown in previous work [22], when the distance between the artery and sensor changes, the pulse signal amplitude and morphology varies, confounding the estimation of dynamic parameters. Therefore, it is critical to study the effect of the electrode location relative to the artery and the distance between electrodes on the measured pulse signal. The pulse signal is affected by the propagation of the current signal injected from the current electrodes through the tissue and the pulsating blood vessels, which generates a voltage distribution in the tissue modulated by the pulse signal. The impedance of the tissue, as well as the artery's diameter and depth, are important factors that affect the measured pulse signal with complex interaction between them. In addition, parameters such as the distance between the electrodes, electrode size, and injection frequency are often selected empirically through experimentation, a long and tedious process. Therefore, there is a need for a better understanding of the current propagation in the tissue and arteries, and their response to the electrical stimulus through accurate modeling of the electrical properties of the tissue and blood flow.

Previous work on Bio-Z modeling and simulation suffered from several limitations. Finite element models (FEM) were

used extensively in modeling bio-impedance of the tissue mainly for tomography and imaging applications. For example, the static impedance of breast and head tissue were modeled for electrical impedance tomography (EIT) using 2D FEM models [23, 24]. In [25], the sensitivity of the voltage measurements due to change in conductivity images was studied using a 2D impedance FEM model for EIT applications. In [26], a 2D static FEM model was developed for Bio-Z using COMSOL to model the artery pulsation for a cross-section of the tissue and the artery. This method considered the pulsation of the artery at a fixed time and did not show time propagation for the arterial wave that can model pulse transit time. On the other hand, circuit models were also used previously to model the electrical properties of the tissue by an impedance network relying on simple circuit analysis and simulation methods such as SPICE, which are fast and easy to use compared to FEM methods [27, 28]. In addition, the tissue circuit model can be augmented with the SPICE models of the sensing circuits to model complex current injections and sensing methods [28, 29]. SPICE simulation was also used to study 2D tissue for EIT applications and breast cancer detection [30, 31]. Previous work based on circuit SPICE models relied on constant impedance values to model the static behavior of the tissue and used simple models for the pulsatile activity inside the arteries which cannot provide a sufficient understanding of the signal distribution inside the tissue and blood flow [32].

The objective of this work is to introduce a fast and reliable method to model the electrical properties of the tissue, blood vessels, and electrical stimulation with realistic parameters to simulate Bio-Z sensing on different parts of the body where the results match measurements.

## III. METHODS

### A. 3D Circuit Model of Tissue

The electrical properties of cells inside tissue and blood vessels can be modeled as an equivalent electrical circuit by resistors  $R_I$  and  $R_E$  and a capacitor  $C_M$ , which represent the intra- and extra-cellular fluid resistance and cell membrane capacitance, respectively, as shown in Fig. 3(a) [33]. The behavior of the resistive and reactive components of tissue impedance across frequency is plotted in Fig. 3(b), which is called Cole-Cole plot. At low frequencies, the body impedance looks resistive ( $= R_E$ ) and decreases to the parallel equivalent of  $R_E$  and  $R_I$  at high frequencies when the cell membrane capacitor shorts. The reactive part is zero at the extreme frequencies and is maximum at  $f_p$ .

The tissue impedance varies with location based on the spatial distribution of the different tissue types such as blood, fat, muscle, and bone. To accurately model this complex tissue impedance and blood flow, we divide the tissue into small 3D elements called voxels for high spatial resolution and assigned a time-varying Bio-Z equivalent circuit  $Z(t)$ . Then, the full tissue model consists of a large 3D network of connected voxels mimicking the physiology of the body and vasculature. This impedance model is a function of space, time, and frequency, denoted as  $Z(x,y,z,t,f)$ , as shown in Fig. 2.

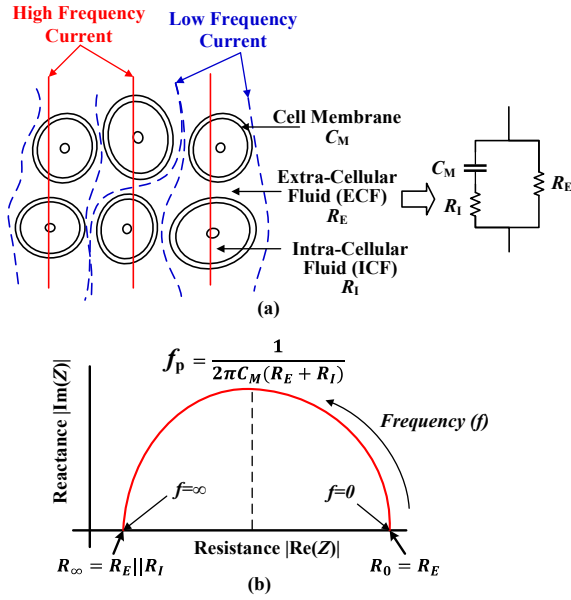


Fig. 3. (a) Cell's equivalent circuit and (b) Bio-Z impedance Cole-Cole plot.

TABLE I  
MODEL PARAMETERS AND THEIR TYPICAL VALUES

Param.	Description	Typical Value
$L$	Length of the impedance voxel	2 mm
$L_x$	Body dimension in X-direction	85 mm
$L_y$	Body dimension in Y-direction	70 mm
$L_z$	Body dimension in Z-direction	38 mm
$A_x$	Artery's location in X-direction (Radial)	23 mm
	Artery's location in X-direction (Ulnar)	67 mm
$A_z$	Artery's depth in Z-direction	2-4 mm
$A_d$	Artery's diameter	2 mm
$PI_x$	Position of lower current electrode in X-direction	23 mm
$PI_y$	Position of lower current electrode in Y-direction	8 mm
$PV_x$	Position of lower voltage electrode in X-direction	23 mm
$PV_y$	Position of lower voltage electrode in Y-direction	16 mm
$S_v$	Spacing between voltage electrodes	10 mm
$S_i$	Spacing between current electrodes	24 mm
$E_x$	Electrode size in X-direction	8 mm
$E_y$	Electrode size in Y-direction	16 mm
$\Delta Z_A$	Radial artery's impedance change	10%
	Ulnar artery's impedance change	5%
$I_s$	Current injection amplitude	0.5 mA
$f_c$	Current injection frequency	10 kHz
$f_{HR}$	Heart rate frequency ( $=1/ BI $ )	1 Hz
$PTT_A$	Pulse transient time between first and last voxel of artery's model	15 ms

The electrical properties of the tissue such as fat, muscle, and bone are static and do not change with time, therefore the tissue voxel consists of static impedance ( $Z_T$ ) with fixed resistors and capacitor ( $R_E$ ,  $R_I$ , and  $C_M$ ) of the cell equivalent circuit, as shown in Fig. 4. However, the pulsation of blood inside arteries is a dynamic activity that changes blood volume with time, thus it is modeled as a time-varying impedance ( $Z_A(t)$ ), as explained later.

The skin-electrode impedance ( $Z_{SE}$ ) consists of multiple layers including the stratum corneum layer inside the skin and

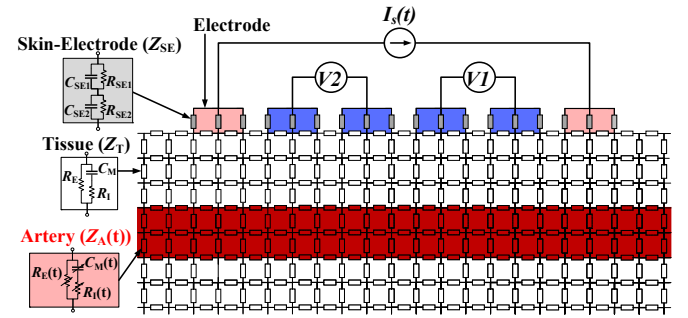


Fig. 4. Cross-section of the proposed circuit grid model illustrating the impedance model for tissue ( $Z_T$ ), artery ( $Z_A(t)$ ) and skin-electrode impedance ( $Z_{SE}$ ).

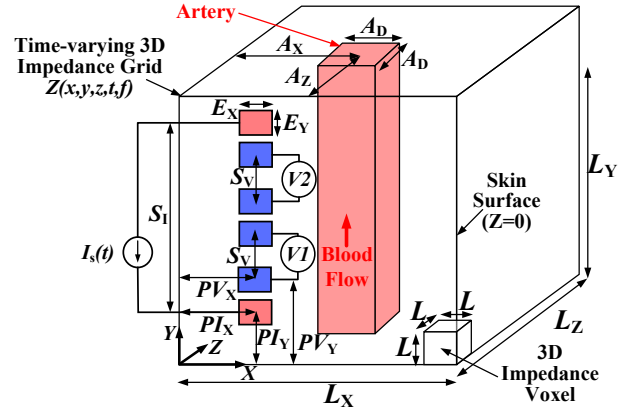


Fig. 5. Geometrical parameters of the circuit model of the wrist and Bio-Z current injection and voltage sensing electrodes with dual voltage channels ( $V1$  and  $V2$ ) for PTT monitoring.

the conductive layer of the electrode [34]. Each layer can be modeled as a parallel resistor and capacitor ( $R_{SE}$  and  $C_{SE}$ ). In our model, we used two layers of RC circuits to represent the skin-electrode impedance, as shown in Fig. 4, as the best fit with our measurement data.  $Z_{SE}$  impedance is connected at the model top layer at each node that is covered by the electrode surface area and then connected together to represent the electrode terminal.

The proposed wrist 3D model simulates the electrical properties of the wrist with its constituent tissues of skin, fat, muscle, and bone according to the anatomy of the wrist. The model includes the blood pulsation and PTT of the radial and ulnar arteries at the wrist. The wrist and blood flow are modeled along the vertical direction ( $Y$ -axis) and the cross-section of the wrist along the  $X$  and  $Z$  axes assuming the skin surface is the  $Z = 0$  plane. The Bio-Z electrodes for current injection and voltage sensing are placed vertically parallel to the arteries with two voltage channels ( $V1$  and  $V2$ ) for continuous monitoring of the blood pulsation and PTT, as shown in Fig. 5. This model is highly parameterized including the geometry of the 3D shape, arteries, voltage and current electrodes, and the spatial resolution of the grid. The complete list of parameters in this model is shown in Table I. This model is generalizable allowing it to be used to model any part of the body, for example, the chest, where time-varying impedance  $Z(t)$  can model the heart and lung movements to simulate the impedance cardiogram and respiration rate, respectively.

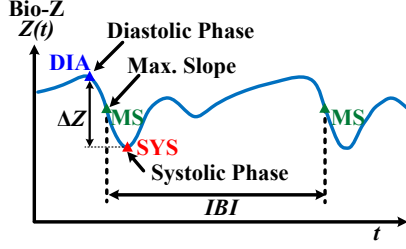


Fig. 6. Typical Bio-Z signal showing the arterial pulse wave with the characteristic points: diastolic peak (DIA), max. slope (MS), and systolic foot (SYS) in addition to inter-beat-interval (IBI).

### B. 3D Circuit Model of the Artery

Each cardiac cycle, the heart pumps blood to the body causing a pressure pulse wave to travel through the arteries. Arterial stiffness controls PTT, which is the time taken by the pressure pulse to travel between two points along the artery. When the heart contracts, the artery's pressure increases from diastolic to systolic pressure which causes expansion of the artery's diameter from  $D_A$  to  $D_A + \Delta D_A$  with an increase of blood volume from  $v$  to  $v + \Delta v$ . The increased blood volume leads to higher conductivity and causes the Bio-Z to decrease by  $\Delta Z$ , as illustrated in Fig. 6 by the sudden drop from the diastolic peak (DIA) to the systolic foot (SYS) passing through the maximum slope point (MS), which are the characteristic points of the Bio-Z cardiac cycle. After the Bio-Z reaches the foot, it increases gradually to the next diastolic peak, which repeats every cardiac cycle with the inter-beat-interval (IBI). A smaller foot exists after some time from the main foot indicating blood reflections that occur due to branching in the arteries. The  $\Delta Z$  reduction in Bio-Z is equivalent to a decrease in the extra- and intra-cellular fluid resistances,  $\Delta R_E$  and  $\Delta R_I$ , and an increase in the cellular membrane capacitance,  $\Delta C_M$ . The increase in blood vessel diameter during the pulsation results in an increase in the cross-sectional area of the blood vessel that is associated with a decrease in the equivalent resistance of the blood vessel according to  $R = \rho L/A$ , where  $\rho$ ,  $A$ , and  $L$  are the blood resistivity, area, and length of the blood vessel, respectively. In addition, the increase in blood volume can be interpreted as an increase in total surface area of the cells which leads to an increase in the equivalent cell membrane capacitance according to  $C = \epsilon A/d$  where  $\epsilon$ ,  $A$ , and  $d$  are the blood permittivity, area of the cell membrane, and its thickness.

$$Z_A(t) = Z_A - \Delta Z_A \sin(2\pi f_{HR}(T - td_i)) \quad (1)$$

$$Z_A(t) = \left\{ \begin{array}{l} R_I - \Delta R_I \sin(2\pi f_{HR}(T - td_i)) \\ R_E - \Delta R_E \sin(2\pi f_{HR}(T - td_i)) \\ C_M + \Delta C_M \sin(2\pi f_{HR}(T - td_i)) \end{array} \right\} \quad (2)$$

$$td_i = \frac{i}{N} PTT_A \text{ for } i = 0 \text{ to } N - 1 \quad (3)$$

In the proposed model, the artery's time-varying impedance  $Z_A(t)$  includes a static component  $Z_A$  modeled by the blood impedance model ( $R_I$ ,  $R_E$ , and  $C_M$ ) in addition to a variable component that changes with time to model blood volume

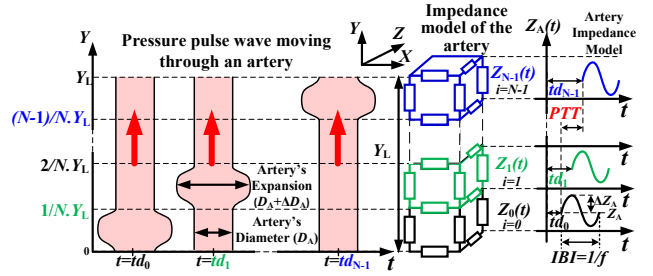


Fig. 7. The proposed 3D model of the artery showing the impedance waveform  $Z_A(t)$  at each voxel of the artery due to blood volume changes with PTT.

changes due to the arterial pulse wave as shown in (1). The variable impedance of the blood pulse is approximated by a sinusoidal waveform that models the change in pulse impedance amplitude of  $\Delta Z_A$  (equivalent to  $\Delta R_E$ ,  $\Delta R_I$ , and  $\Delta C_M$ ) at heart rate frequency  $f_{HR}$ , which is the inverse of IBI. We used the approximate sinusoidal waveform for impedance and voltage pulses because we focus on the peak-to-peak changes in voltage due to impedance change rather than the morphology of the pulse signal and to simplify the estimation of the delay of the voltage pulse signal. The artery's model equations are shown in (2) for each resistive and capacitive component of the artery's circuit model. The model is unique in considering both the spatial and temporal properties of blood flow, which allows modeling of the PTT that is related to arterial stiffness and essential for the estimation of hemodynamic parameters such as BP. To model PTT, each 3D voxel along the artery's location is assigned a delayed sinusoidal impedance waveform of delay  $td_i$  that increases linearly along the direction of blood flow as in (3) from  $i = 0$  to  $N - 1$ , where  $i$  is the voxel index,  $N$  is the total number of artery's voxels in the Y-direction, and  $PTT_A$  is the total delay of the pulse from the first to the last voxel along the artery, as shown in Fig. 7. Despite using a linear blood flow model as an example, our modeling approach is flexible and can use any input model for the blood volume changes with non-linear function for each voxel in our 3D model. This approach allows applying any non-linear blood flow model by integrating a non-linear mechanical model with our electrical model for a more complicated and realistic artery model.

### C. Model Parameter Selection

The model parameters were selected to represent the wrist tissue and arteries with Bio-Z sensor for measuring PTT from wrist arteries through two voltage sensors  $V1$  towards the elbow and  $V2$  towards the hand, as shown in Fig. 8. The geometrical parameters of the model were chosen to reflect a simplified 3D model of the wrist anatomy. In literature, the anatomy of the wrist shows the distribution of the different tissue types and the location of the radial and ulnar arteries in the wrist, as shown in Fig. 8(a). The anatomy of the wrist was approximated by the proposed allocation of the tissue such as muscle, fat, and bone, as shown in the impedance map of the wrist as illustrated in the 2D cross-section and 3D plots in Fig. 8 (b, c, and d). We chose the impedance grid resolution (voxel size) to be  $L = 2$  mm to balance between the spatial resolution and simulation

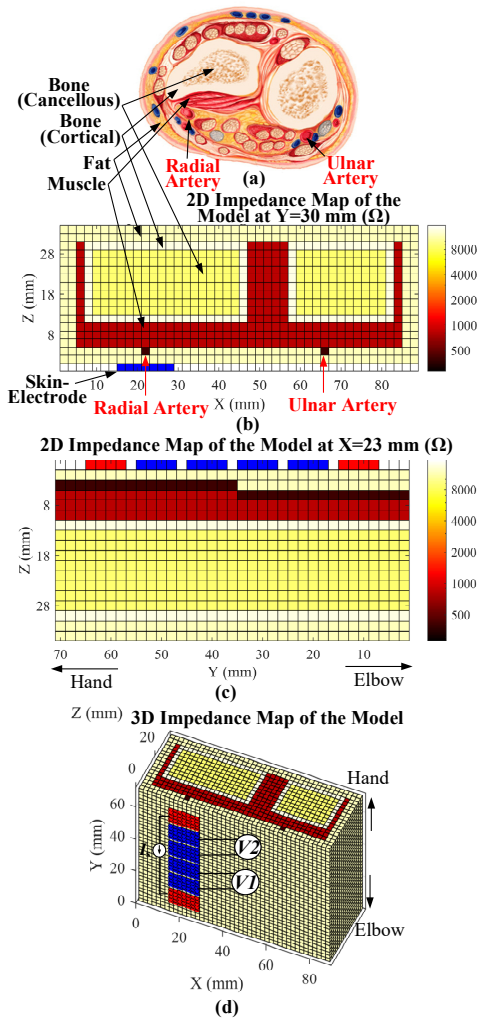


Fig. 8. Proposed wrist circuit model: (a) cross-section of the wrist anatomy, (b) 2D impedance map of the model at  $Y = 30$  mm, (c) 2D impedance map at  $X = 23$  mm, and (d) 3D impedance map.

complexity. The size and the depth of the radial and ulnar arteries were selected to be  $D_A = 2$  mm and  $Z_A = 4$  mm, respectively, according to previous work that studied the average parameters of the radial artery of the wrist from 44 human subjects [35]. This study shows that the artery's depth increases towards the elbow. This depth variation was included in the model by increasing the depth of the arteries in the model from 2 to 4 mm in the lower half of the  $Y$ -direction of the model when the artery is closer to the elbow as shown in Fig. 8(c). The dimensions and location of electrodes were selected to match the experimental results where electrodes for current injection and dual voltage sensing are typically placed over the radial artery as shown in Fig. 8(d).

The DC impedances of tissue and blood were selected based on the electrical properties of conductivity and permittivity for each tissue type that changes with the biological structure of the tissue and frequency ranges. Each frequency range exhibits its characteristic response which is represented by distributions of relative permittivities in complex function in frequency called the Cole-Cole equation as follows

$$\hat{\epsilon}(\omega) = \epsilon_{\infty} + \sum_n \frac{\Delta\epsilon_n}{1 + (j\omega\tau_n)^{1-\alpha_n}} + \frac{\sigma}{j\omega\epsilon_0} \quad (4)$$

TABLE II  
COLE-COLE MODEL PARAMETERS FOR BLOOD [36]

$\epsilon_{\infty}$	$\Delta\epsilon_1$	$\tau_1$ (ps)	$\alpha_1$	$\Delta\epsilon_2$	$\tau_2$ (ps)	$\alpha_2$	$\sigma$
4.0	56.0	8.38	0.10	5200	132.63	0.1	0.7

TABLE III  
IMPEDANCE PARAMETERS OF CIRCUIT MODELS FOR FREQUENCY RANGE 1-100 kHz AND VOXEL LENGTH  $L=2$  mm

Tissue Type	$R$ (kΩ)		$C$ (nF)		$Z$ (kΩ) @ 10 kHz	Avg. Error (%)
	$R_E$	$R_I$	$C_M$	-		
Blood	0.4	1.0	0.164	-	0.4	0.0
Muscle	0.8	4.3	0.468	-	0.8	3.2
Bone Cancellous	8.7	85.3	0.034	-	8.7	1.7
Fat	13.4	93.2	2.090	-	11.7	1.9
Bone Cortical	13.8	95.6	0.009	-	13.8	0.7
Skin-Electrode	$R_{SE1}$	$R_{SE2}$	$C_{SE1}$	$C_{SE2}$	61.3	4.9
	1045.0	24.2	0.293	0.025		

where  $\epsilon_{\infty}$  is the high-frequency permittivity,  $\sigma$  is the tissue conductivity,  $\epsilon_0$  is the permittivity of free space,  $\omega$  is the angular frequency, and each frequency range is defined by its  $\Delta\epsilon_n$  as the low-frequency permittivity,  $\tau_n$  is the characteristic relaxation time,  $\alpha_n$  is the distribution parameter. The Cole-Cole parameters that simulate the electrical properties of the tissue based on experimental measurements are published in [36] for each tissue type and an example for the blood is shown in Table II. The conductivity and permittivity of blood are plotted in Fig. 9(a) versus frequency from 1 Hz to 100 GHz showing their variations with frequency and its Cole-Cole plot is illustrated in Fig. 9(b), which is real versus the imaginary impedance as calculated from the complex permittivity in (4).

We estimated the DC impedance parameters of our circuit model ( $R_I$ ,  $R_E$ , and  $C_M$ ) for each tissue type by fitting to the Cole-Cole model in (4) for a certain frequency range using non-linear least-square curve fitting. The Levenberg-Marquardt method was used for curve fitting by minimizing error for the real, imaginary and magnitude components of the impedance. The estimated DC impedance parameters of our circuit model ( $R_I$ ,  $R_E$ , and  $C_M$ ) for each tissue type for the frequency range 1-100 kHz are listed in Table III.

The impedance error between the circuit model and the Cole-Cole model varies for tissue type and the selected frequency range based on how the tissue Cole-Cole plot is like the theoretical model. To illustrate this variation, we estimated three circuit models for blood for different frequency ranges, as shown in Fig. 9(b). The first and third circuit models showed smaller errors compared to the second model, as shown in Table IV, since the Cole-Cole plot is like the theoretical shape for these frequency ranges. This explains the variation in error for the different models and the mismatch in the Cole-Cole plots for the different tissue types used in the model, as shown in Fig. 9(c). The model accuracy is evaluated by the average error in impedance between our circuit model and the reference

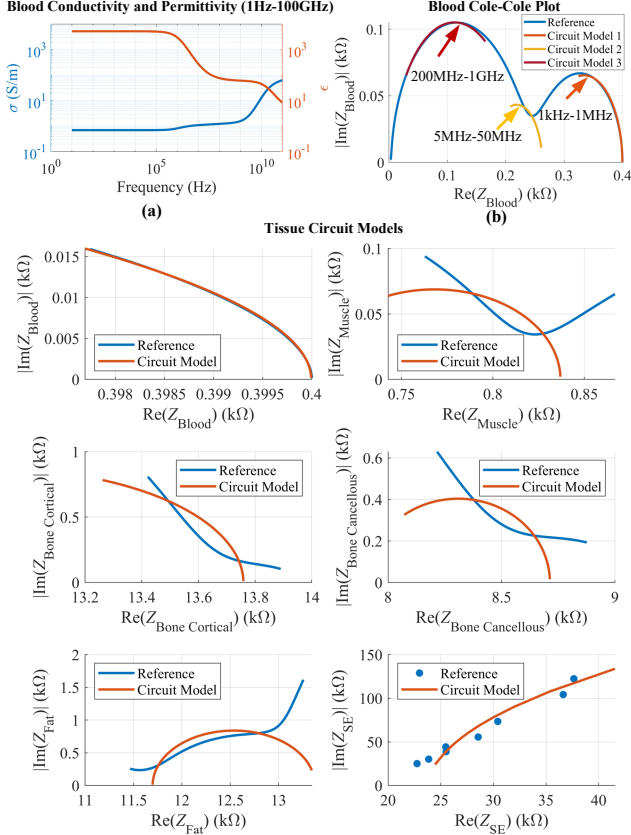


Fig. 9. (a) Blood conductivity and permittivity (1Hz-100GHz), (b) blood Cole-Cole plot and three different circuit models, and (c) Cole-Cole plot of the real and imaginary components of the tissues (1 – 100 kHz) and skin-electrode impedance (3 – 25 kHz), as estimated by the circuit model versus the reference Cole-Cole model.

which varies with tissue type and is less than 5% as shown in Table III. The error is acceptable because it has a small effect on Bio-Z voltage that is linearly proportional to the equivalent impedance and the voltage error will be upper-bounded by this small error value. For future improvements, multiple circuit models can be used for each tissue type for different frequency ranges to minimize the error and extend the frequency range of the simulations.

The skin-electrode impedance parameters ( $R_{SE1}$ ,  $R_{SE2}$ ,  $C_{SE1}$ , and  $C_{SE2}$ ) were estimated by fitting the model to experimental data that were collected from wet electrodes in our lab for discrete frequency points in the range from 3 to 25 kHz. The resistor and capacitor values shown in Table III are scaled for voxel length  $L=2$  mm that is used in the proposed model by multiplying the resistance and dividing the capacitance by a scaling factor estimated from fitting the electrode voltage simulation results with the actual measurements. In Table III, the values of the estimated circuit model are presented with the impedance value at 10 kHz for each tissue type. The impedance of blood is the smallest, followed by muscle, cancellous bone (inner bone), fat, cortical bone (outer bone), and finally the skin-electrode is the highest impedance as expected.

The amplitude of the artery's variable impedance component,  $\Delta Z_A$ , represents the mechanical properties of arterial blood flow such as arterial stiffness and wall thickness, etc.,

TABLE IV  
IMPEDANCE PARAMETERS FOR BLOOD CIRCUIT MODELS FOR  
VOXEL LENGTH  $L=2$  mm

Blood Circuit Model	Frequency Range	R (k $\Omega$ )		C (pF)	Avg. Error (%)
		$R_E$	$R_I$	$C_M$	
Circuit Model 1	0.001 – 1 MHz	0.4	0.82	15.3	0.18
Circuit Model 2	5 – 50 MHz	0.26	0.5	5.2	5.1
Circuit Model 3	0.2 – 1GHz	0.22	0.007	2.0	1.97

which are not represented by the other geometrical and electrical parameters in our model and varies between radial and ulnar arteries and from one subject to another. The parameter  $\Delta Z_A$  affects the pulsatile activity of the artery and affects the voltage pulse amplitude  $\Delta V_{pp}$ . We estimated an average  $\Delta Z_A$  as a ratio of blood impedance  $Z_{Blood}$  based on experimental measurements for each subject by iteratively minimizing the error of the average  $\Delta V_{pp}$  between the simulation results and measurements while changing the sensing location across the wrist. From literature, the pulsatile activity of the radial artery is larger than the ulnar artery which is supported by our choice of larger  $\Delta Z$  for the radial artery of 10% compared to 5% for the ulnar artery [37]. We selected  $PTT_A = 15$  ms for the artery's model to match the experimental measurements of PTT across the same distance on the wrist.

#### D. Simulation Flow

The proposed 3D circuit model is based on a SPICE netlist with a large network of resistors and capacitors. The Bio-Z simulation platform uses MATLAB to generate the SPICE netlist with a 3D grid of time-varying impedances  $Z(x,y,z,t,f)$  and current source  $I_s(t)$  according to the model parameters, as shown in Fig. 10(a). In the SPICE netlist, the current source is connected to the assigned nodes of the current electrodes through the skin-electrode impedance. The effect of electrode size is modeled by connecting all the nodes within the area of the electrodes at the specified electrode location on the surface plane of the 3D model,  $Z = 0$ . Then, MATLAB invokes LTSPICE to run the simulation with the specified simulation options (e.g., simulation time, time step, and start and stop frequencies for frequency analysis). Post simulation, MATLAB reads the LTSPICE results that contain the voltage at each node and the current through each element and arranges the data in a multi-dimensional array,  $V(x,y,z,t,f)$  and  $I(x,y,z,t,f)$  that maps to the 3D grid for post-processing, as shown in Fig. 10(a). The resulting sensor voltages,  $V1$  and  $V2$ , are calculated by the difference of the voltage between the electrodes. A current vector  $\vec{I} = \langle I_x, I_y, I_z \rangle$  is calculated at each node from the equivalent current in each dimension, as shown in Fig. 10(b).

The simulation time needs to be at least one period of a heartbeat ( $\sim 1$  s) to simulate the low-frequency variation of blood flow at  $f_{HR}=1$  Hz simultaneously with the high-frequency current injection signal at  $f_c$  from 1 to 100 kHz. This transient simulation will take a long time because of the small simulation time step required by the high-frequency current signal. Furthermore, synchronous IQ demodulation must be performed

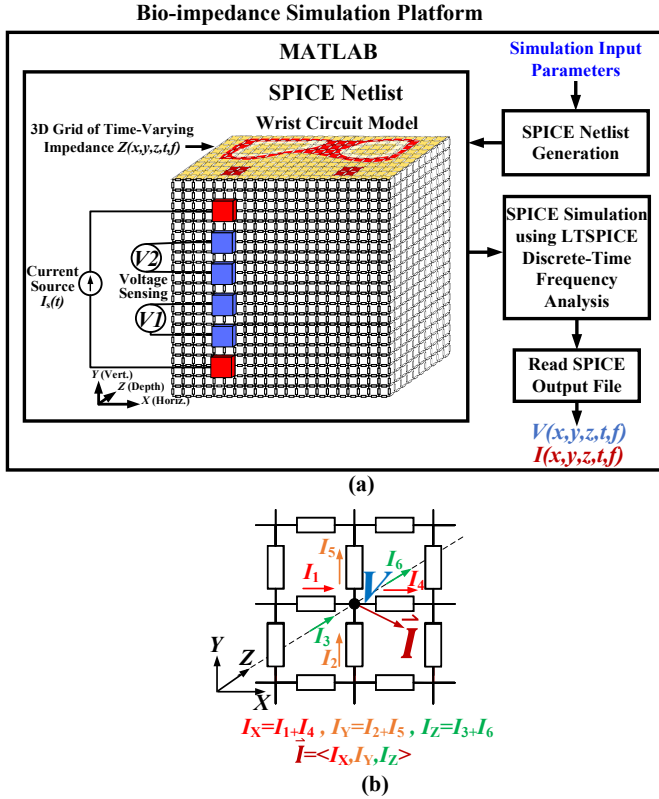


Fig. 10. (a) The simulation flow for the circuit model using SPICE simulation and MATLAB for the generation of voltage and current distributions, (b) current vector ( $\vec{I}$ ) calculation at each node of the circuit model.

to extract the complex impedance signal from the amplitude and phase of the AC voltage signal. Therefore, we used a series of fast AC analysis (.ac) SPICE simulations at different time steps to mimic the AC response of the circuit at a specific frequency for the full pulse period to get the complex impedance values. This is repeated for 8-time steps in the pulse period using a different netlist for each time step that reflects the change in the values of resistors and capacitors with time steps according to the model of the blood volume changes due to the arterial pulse. Afterward, the results are concatenated in time to form the voltage signal,  $V_{sim}(t)$ . The proposed stepwise AC analysis provides more control over the time steps and is more than 200x faster in simulation time compared to the transient analysis that uses variable time steps. This approach assumes independence between the AC responses at the different time steps because the changes in impedance because of the pulse signal is very slow compared to the time constant of the resistors and capacitors of the tissue which is validated by a transient simulation that matches our AC simulation as shown later.

The simulated Bio-Z voltage signal,  $V_{sim}(t)$ , consists of a DC component,  $V_{dc}$ , and an AC component,  $\Delta V$  generated from impedance changes  $\Delta Z$  from the pulse wave, as shown in Fig. 11(a).  $V_{sim}(t)$  is a sinewave with different amplitudes and delays that is affected by the transfer function of the model and the sensing configuration. The amplitude  $\Delta V_{pp}$ , DC offset  $V_{dc}$ , and delay  $T_d$  of the voltage signal were estimated using a regression

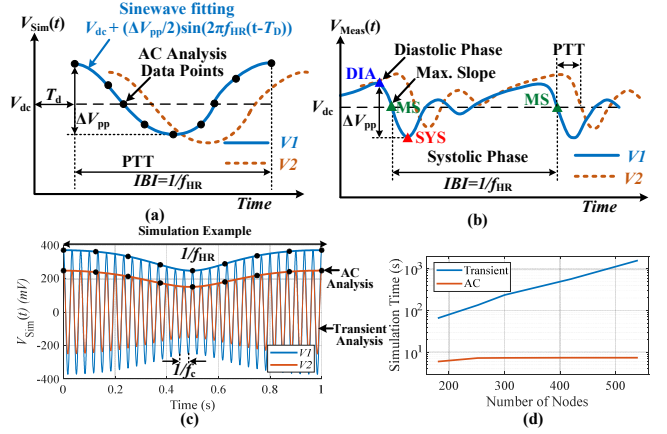


Fig. 11. (a) Voltage signals from AC analysis,  $V_{sim}(t)$ , (b) actual Bio-Z voltage signals,  $V_{meas}(t)$ , showing the DC and AC components,  $V_{dc}$  and  $\Delta V_{pp}$ , respectively in addition to pulse time delay ( $T_d$ ) and pulse transit time (PTT) between  $V1$  and  $V2$ , (c) SPICE simulation example for the voltage signals with transient versus AC analysis with  $f_{HR} = 1$  Hz and  $f_c = 30$  Hz, (d) simulation time of transient and AC analysis versus number of nodes

model that fits the measured data to the expected sinewave with variable parameters as in

$$V_{sim}(t) = V_{dc} + \left( \frac{\Delta V_{pp}}{2} \sin(2\pi f_{HR}(T - T_d)) \right) \quad (5)$$

The parameters are estimated by minimizing the RMSE error between the readings and (5). The PTT is calculated from the difference of time delay  $T_d$  between  $V1$  and  $V2$ .

We carried out a comparison between the proposed stepwise AC analysis and the alternative transient analysis by the simulation of a simple model with small dimensions of 8x28x6 mm, single-node electrodes,  $f_{HR} = 1$  Hz, and  $f_c = 30$  Hz to validate the stepwise AC analysis approach and to show the relation between the output signals. The SPICE netlist for the transient analysis included the resistors and capacitors expressed as time functions as in (2), which results in a high-frequency signal at  $f_c$  modulated with the Bio-Z in its amplitude and phase at the low heart rate frequency  $f_{HR}$ . However, the proposed stepwise AC analysis method results in the modulated Bio-Z signal directly that matches the envelope of the transient analysis for both  $V1$  and  $V2$  which validate our AC simulation approach as shown in Fig. 11(c). The simulation time for our proposed AC analysis and transient analysis are plotted in Fig. 11(d) versus the number of nodes of the model for the simulation of one heart pulse period for one second with carrier frequency  $f_c = 10$  kHz. The simulation of AC analysis is 200x faster compared with transient analysis with 7.36 seconds for AC analysis and 1,588 seconds for transient analysis for a model with 540 nodes because the transient analysis requires 240k time steps compared to only 8-time steps for our proposed AC analysis. The simulation time of the transient analysis increases at a higher order versus the number of nodes and requires 116x more storage compared to the AC analysis which makes transient analysis prohibitively expensive for models with a larger size. Therefore, the proposed model allows efficient Bio-Z simulation both in time and frequency.

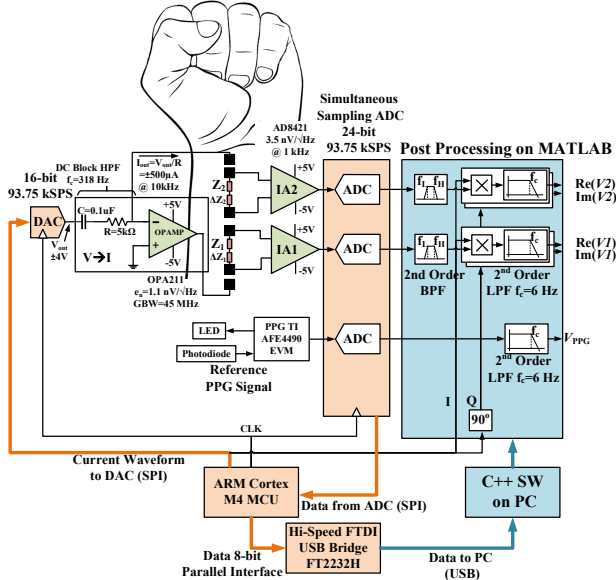


Fig. 12. Block diagram of custom Bio-Z measurement hardware and algorithms that depends on IQ demodulation for extracting the real and imaginary parts of Bio-Z with dual voltage channels of  $V_1$  and  $V_2$  for PTT measurements.

### E. Bio-Z Measurement System

For validation between the simulation and measurement results, we carried out an extensive characterization of the Bio-Z signal for different configurations. The characterization was done by measuring Bio-Z from the wrist using custom hardware and signal processing algorithms that are capable of measuring multi-channel, high-resolution impedance signal that captures the pulse signal due to blood volume changes in the wrist arteries, as shown in Fig. 12 [14]. The Bio-Z measurement system has a high sampling rate of 93.75 kSPS to measure small PTT values. We extract Bio-Z voltage based on synchronous IQ demodulation to get both the real and imaginary components with programmable frequency from 3 to 25 kHz. Using the current injection signal for Bio-Z at 10 kHz compared to the low-frequency flicker noise provides higher immunity to noise and 60 Hz interference compared to other baseband physiological signals such as ECG and EEG. Our measurement system includes a PPG signal from the finger using an optical finger clip that is measured simultaneously with the Bio-Z channels to provide a reference for the pulse signal.

Values for  $V_{dc}$  and  $\Delta V_{pp}$  based on the average beat-to-beat values over a period were calculated from the measured data based on the 3 characteristic points detected in each cardiac cycle (DIA, MS, and SYS). These points were detected based on the peak, foot, and zero-crossing points of the first derivative of the signal [14].  $V_{dc}$  is the voltage of MS point, while  $\Delta V_{pp}$  is the difference between the voltage of DIA and SYS points, as shown in Fig. 11(b). PTT is measured by the time difference between MS points of  $V_1$  and  $V_2$  signals. All values are calculated by the average over all valid heart beats within the data collection time. To evaluate the accuracy of the measured pulse signal, the inter-beat-interval RMSE relative to a reference signal measured from a clip-on PPG sensor was

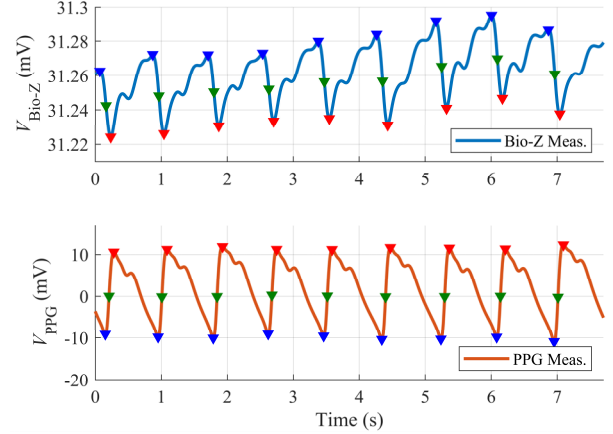


Fig. 13. Measured Bio-Z signal ( $V_{Bio-Z}$ ) and PPG signal ( $V_{PPG}$ ) showing the DIA (blue), MS (green), and SYS (red) points.

calculated. PPG from the finger was chosen as a reliable reference for the arterial pulse signal at the wrist because the measured light signal is focused on a single artery in the finger and measures the blood volume changes of the finger's artery from the transmission of the light through the artery. Furthermore, the pulse signal at the finger is measured at a very short distance after passing through the wrist arteries, which is a good approximation for the arterial signal at the wrist. The IBI for Bio-Z and PPG signals were measured by the difference between each successive MS point. When the IBI RMSE increases, this indicates a less accurate and noisy Bio-Z pulse signal. An example of the measured Bio-Z and PPG signals are shown in Fig. 13, highlighting the DIA, MS, and SYS points for each signal that were used to calculate  $V_{dc}$ ,  $\Delta V_{pp}$ , and the IBI RMSE. The PPG pulse signal is the opposite of the Bio-Z because higher PPG voltage means larger blood volume.

## IV. RESULTS

In this section, we show the simulation results of  $V_{dc}$ ,  $\Delta V_{pp}$  and PTT for the proposed wrist circuit model versus changing the voltage electrodes location, the current injection location relative to the artery, electrode size, and the current injection frequency, validated by Bio-Z measurements from the wrist. We collected Bio-Z data from multiple human subjects under Texas A&M University IRB (IRB2017-0086D). The actual location of the wrist arteries was detected using a Huntleigh Doplex MD2 Bi-Directional Doppler, which measures arterial blood flow using a probe with high spatial sensitivity. For the Bio-Z measurement settings, we used current injection with typical values as used in simulation with an amplitude of 0.5 mA at a frequency of 10 kHz, which are compliant with safety standards [38]. There are expected variations from one subject to another because of anatomical differences in the tissue and arteries. Therefore, we developed our conclusions based on the average data from multiple subjects. In addition, there is a normal variation across the different parameter steps due to physiological changes that occurs over time or due to motion artifacts. Despite careful considerations to minimize these effects, these variations may occur and therefore we use a polynomial curve fitting to extract the trend of our

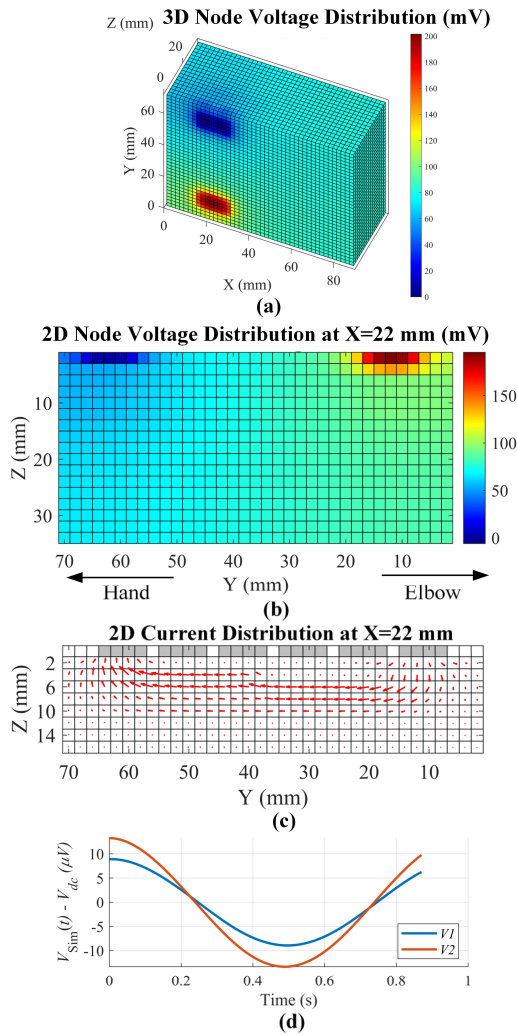


Fig. 14. Voltage and current simulation results: (a) 3D voltage distribution of the tissue, (b) 2D voltage distribution at  $X = 22$  mm, (c) 2D current distribution at  $X = 22$  mm, and (d) the sensor voltage signals ( $V1$  and  $V2$ ) with variation over time due to blood flow. [16]

measurements versus the target parameter that is compared with our model.

#### A. Simulation Example

Fig. 14 illustrates the voltage and current distribution using the typical simulation value as resulted from the proposed model shown in Fig. 8. The 3D voltage distribution at each node in the tissue model shows a maximum voltage of 200 mV at the location of the input current electrode (closer to elbow at  $Y = 12$  mm) relative to the other current electrode (closer to hand at  $Y = 62$  mm) with the minimum voltage, as shown in Fig. 14(a). The voltage changes gradually in the tissue going away from the current electrodes in the three dimensions approaching the middle voltage range of around 100 mV as shown in the 2D voltage distribution at  $X = 22$  mm in Fig. 14(b). The current vector distribution inside the tissue is plotted by red arrows with arrow's length proportional to the current amplitude, as shown in Fig. 14(c). The current flows inside the tissue between the current electrodes with maximum current amplitude at the artery's location because of the lower impedance of blood

TABLE V  
SIMULATION RESULTS OF VOLTAGE SENSORS

Voltage Sensor	$V_{dc}$ (mV)	$\Delta V_{pp}$ ( $\mu$ V)	$T_d$ (ms)
$V1$	49.02	17.84	3.53
$V2$	39.72	26.63	10.94

compared to the other tissues of the wrist. The  $V_{dc}$  simulation result of voltage sensor  $V2$  is 39.72 mV, which is lower than  $V1$  with  $V_{dc}$  of 49.02 mV because of the closer artery at  $V1$  compare to  $V2$ , which reduces the impedance and  $V_{dc}$  as shown in Table V. The variable component of  $V1$  and  $V2$  due to blood flow are plotted versus time in Fig. 14(d) with a sinusoidal waveform as a response to the artery's variable impedance model with large  $\Delta V_{pp}$  of 26.63  $\mu$ V for  $V2$  compared to 17.84  $\mu$ V for  $V1$  due to closer artery at  $V2$ . The pulse arrival time at  $V1$  and  $V2$  is estimated from the time delay  $T_d$  as 3.53 and 10.94 ms for  $V1$  and  $V2$  respectively that shows the direction of blood pulse along the artery in the  $Y$ -direction from  $V1$  to  $V2$ . The results of this simulation illustrate the operation of the model as expected that can capture the electrical properties of the tissue and the blood flow.

#### B. Effect of Voltage Electrode Location

We studied the effect of electrode position on  $V_{dc}$  and  $\Delta V_{pp}$  by changing the horizontal and vertical location of the voltage electrodes as well as the spacing between them while fixing the current electrode's location. Simulations were validated against human subject ( $n = 3$ ) Bio-Z measurements by taking the average of data collected over 3 minutes at each position. To study the effect of voltage electrode spacing, we placed two pairs of wet electrodes ( $1.6 \times 0.85$  cm<sup>2</sup>) aligned on the radial artery of the wrist. The spacing ( $S_V$ ) between the voltage electrodes was varied from 1.5 to 6 cm, centered around the midpoint between the current electrodes, which were 9 cm apart. Both simulations and measurements showed an increase in  $V_{dc}$  and  $\Delta V_{pp}$  with increasing  $S_V$ , as shown in Fig. 15(a).

The effect of the vertical location of the voltage electrodes relative to current electrodes was also studied. Current electrodes were placed with 7.5 cm spacing while changing the vertical location of the voltage electrodes ( $PV_Y$ ) from 1.5 to 6 cm relative to the upper current electrode, as shown in Fig. 15(b), with a spacing of 1.5 cm between them. Both simulations and measurements showed a minimum in  $V_{dc}$  and  $\Delta V_{pp}$  when the voltage electrodes were in the middle and a peak when the voltage electrodes were closer to the current electrodes (minimum and maximum  $PV_Y$ ) because of higher current amplitude near the current electrodes compared to the middle. Measurements and simulations showed a lower  $V_{dc}$  peak towards the hand (larger  $PV_Y$ ) because of the smaller artery's depth with a lower impedance of blood closer to the skin that decreases voltage compared to the other side towards the elbow. However,  $\Delta V_{pp}$  showed a higher peak towards the hand because of the small depth of the radial artery towards the hand which results in more pulsation compared to the other side of the wrist towards the elbow.

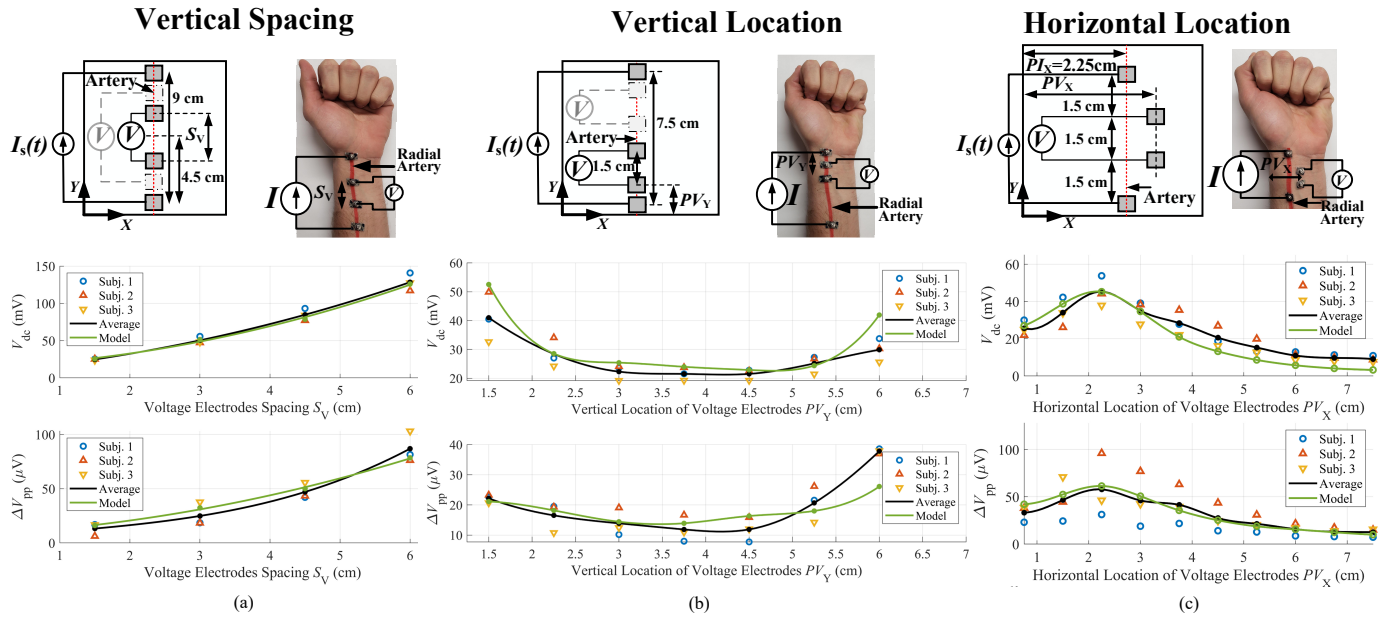


Fig. 15. Comparison between the simulated and measured  $V_{dc}$  and  $\Delta V_{pp}$  for different (a) voltage electrode spacing  $S_V$ , (b) vertical location of voltage electrodes  $P_{V_Y}$ , and (c) horizontal location of voltage electrodes  $P_{V_X}$ .

To study the effect of the horizontal location of voltage electrodes  $P_{V_X}$ , we placed wet electrodes ( $0.85 \times 0.85 \text{ cm}^2$ ) on the radial artery ( $P_{I_X} = 2.25 \text{ cm}$ ) of the wrist with 4.5 cm spacing between the current electrodes while changing the horizontal distance of the voltage electrodes  $P_{V_X}$  from 1.5 cm at the left of the radial artery ( $P_{V_X} = 0.75 \text{ cm}$ ) to 5.25 cm at the right of the artery ( $P_{V_X} = 7.5 \text{ cm}$ ) with 1.5 cm spacing between the voltage electrodes. Both measurements and simulations showed a peak in  $V_{dc}$  and  $\Delta V_{pp}$  when the voltage electrodes are aligned with the current electrodes ( $P_{V_X} = 2.25 \text{ cm}$ ) and they decrease as  $P_{V_X}$  increases, as shown in Fig. 15(c). It can be concluded from these results that  $V_{dc}$  and  $\Delta V_{pp}$  can be maximized if the voltage electrodes are placed as close as possible to the current electrodes at the artery's location.

### C. Effect of Sensing Location Relative to the Artery

For accurate estimation of hemodynamic parameters using wearable devices, it is important to understand the effect of sensing location relative to the artery on the quality of the sensed pulse signal. In this experiment, we show the simulation and measurement results of  $\Delta V_{pp}$  of the pulse signal and IBI RMSE for changing the Bio-Z sensing location including the current and voltage electrodes horizontally with a fine step on the wrist from the radial to the ulnar artery.

We used a custom wrist band that includes an array of 8 columns and 6 rows of silver electrodes with size  $5 \times 5 \text{ mm}$  and spacing of 3 mm. Each column consists of 6 electrodes for current injection and simultaneous monitoring of two voltage channels ( $V1$  &  $V2$ ). Measurements repeated for 8 different sensing locations at each column with horizontal sensing location  $P_{I_X}$  varies from 8 to 62 mm on the wrist with a small step of 8 mm. Data was collected from 3 participants for 5 minutes at each sensing location. The average location of the radial artery for participants was between columns 2 and 3 ( $P_{I_X} = 16$  to 24 mm), while the ulnar artery was located around

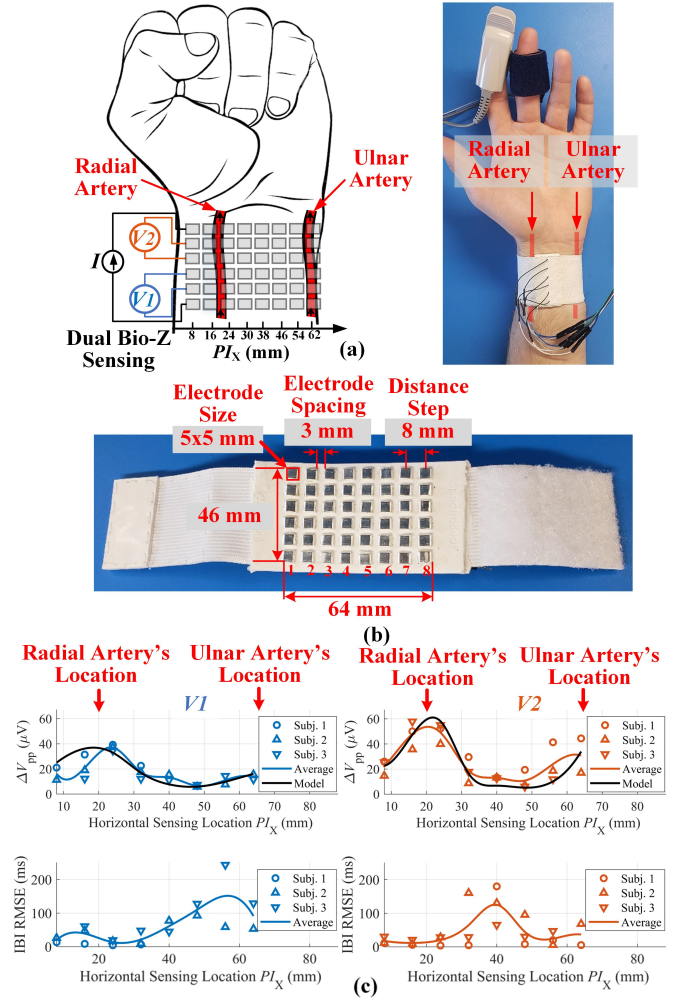


Fig. 16. The effect of sensing location on pulse signal: (a) the location of the electrode array on the wrist, (b) picture of the custom electrode array wrist band, (c) the measurements and model results of  $\Delta V_{pp}$  and IBI RMSE versus horizontal sensing location  $P_{I_X}$ .

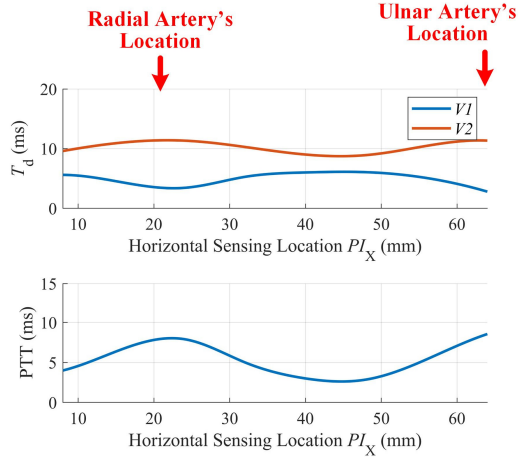


Fig. 17. Simulation results of the voltage signal delay  $T_d$  for  $V1$  and  $V2$  (top), and PTT between  $V1$  and  $V2$  versus horizontal sensing location  $PI_X$ .

column 8 ( $PI_X = 62$  mm) as shown in Fig. 16(a, b). The 3D simulation model used the same dimensions for the sensing locations and electrode size quantized by  $L = 2$  mm.

The measurement results in Fig. 16(c) shows the variation of  $\Delta V_{pp}$  amplitude versus the horizontal sensing location  $PI_X$  for each subject in addition to the calculated average of all subjects. For the upper voltage channel closer to the hand ( $V2$ ), there is a significant peak of  $\Delta V_{pp} = 60$   $\mu V$  around the location of the radial artery at  $PI_X = 20$  mm and a smaller peak of  $30$   $\mu V$  at the location of the ulnar artery at  $PI_X = 62$  mm, because of the weaker pulsation of the ulnar artery compared to the radial artery. The voltage channel  $V1$  towards the elbow shows a similar trend for  $\Delta V_{pp}$ , but with smaller amplitude because of the larger depth of arteries under the skin towards the elbow.

It is important to maximize the amplitude of  $\Delta V_{pp}$  to achieve the best quality of pulse signal that leads to accurate detection of fiducial points and IBI for reliable hemodynamic parameter estimation. The IBI RMSE of this measured data was minimum with 10 ms at the peak of  $\Delta V_{pp}$  at  $PI_X = 20$  as shown in Fig. 16(c). When the amplitude of  $\Delta V_{pp}$  decreases at the location between the arteries, the signal becomes noisy which degrades the quality of characteristic point detection and results in high IBI RMSE of around 150 ms. This shows the significant effect of the sensing location relative to the artery on the quality of the pulse signal and the importance of selecting the right sensing location close to the artery for the best physiological monitoring of cardiac signals.

The model simulation results of  $\Delta V_{pp}$  versus  $PI_X$  matches exactly the measurement results for both  $V1$  and  $V2$  which shows the capability of the proposed model to accurately simulate the effect of sensing location relative to both radial and ulnar arteries taking into consideration the different behavior for both arteries and both voltage channels  $V1$  and  $V2$ .

#### D. PTT Variation with Sensing Location

One of the important outcomes of the proposed model is understanding how the measured PTT changes with the sensing location since the PTT measured from the delay between the voltage sensors is affected by the tissue between the artery and

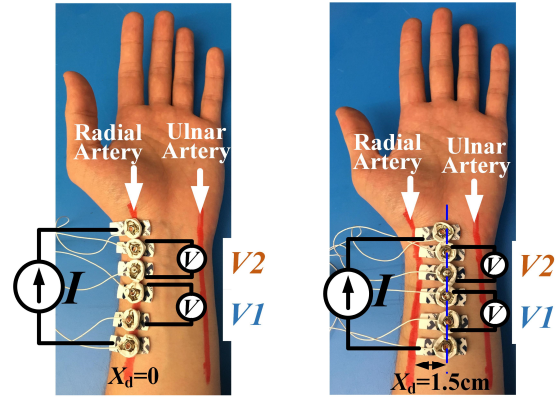


Fig. 18. Pictures of electrode placement for validating the effect of sensing location on the PTT by dual channel Bio-Z measurements with sensing location  $X_d = 0$  and 1.5 cm relative to the radial artery.

TABLE VI  
PTT AND AMPLITUDE MEASUREMENTS WITH  $X_d = 0$  AND 1.5 CM

	$X_d$	Subj.	1	2	3	4	5	Mean
PTT (ms)	0	Mean	8.0	3.0	6.8	8.2	7.9	6.8
		STD	3.8	2.7	1.8	3.0	4.3	3.1
	1.5	Mean	3.4	-2.6	11.1	5.6	-2.5	3.0
		STD	7.0	4.9	2.9	5.2	7.9	5.6
$\Delta V_{pp}$ ( $\mu V$ )	0	Mean	33.1	33.9	56	52.4	27.4	40.6
		STD	10.1	5.8	6.2	10.2	5.5	7.5
	1.5	Mean	26.3	19.9	32.6	26.1	22.3	25.4
		STD	7.5	2.9	3.0	5.7	4.5	4.7

the sensors. Based on the previous simulation, we extracted the time delay information  $T_d$  representing the arrival time of the pulse wave at each voltage channel ( $V1$  and  $V2$ ) versus the horizontal sensing location  $PI_X$ , shown in Fig. 17, with artery's model  $PTT_A$  equal to 15 ms. The simulation results show that the pulse arrival time changes with  $PI_X$  by reaching the  $T_d$  of 3.4 ms for  $V1$  and 11.4 ms for  $V2$  at the arteries' location according to the direction of pulse wave flow. While at the middle distance between the arteries,  $T_d$  approaches half of  $PTT_A$  of 7.5 ms because of the averaging effect of the tissue that leads to similar timing information for  $V1$  and  $V2$  as they go further from the arteries. Therefore, the maximum PTT is 8 ms at the arteries location and the minimum is 2.6 ms in the middle of the arteries. This shows the importance of sensing location to be close to the artery to achieve the maximum sensitivity of PTT.

We compared the PTT results from the simulation model with the experimental measurements of PTT measured from a larger Bio-Z sensor to provide large signal amplitude away from the artery that allows the detection of the characteristic points to estimate PTT accurately. We used six wet electrodes with size  $0.8 \times 1.6$   $cm^2$  with a spacing of 10 mm between every two electrodes for measuring  $V1$  and  $V2$  and estimate PTT from the time delay between the MS points. The electrodes were placed on the radial artery and between the radial and ulnar artery with the sensing distance from the artery is  $X_d = 0$  and 1.5 cm, as shown in Fig. 18. The data was collected from 5 subjects with 5 minutes per subject and  $\Delta V_{pp}$  and PTT were calculated for the average across all heart beats, as shown in Table VI which has the mean and standard deviation (STD) of the Bio-Z

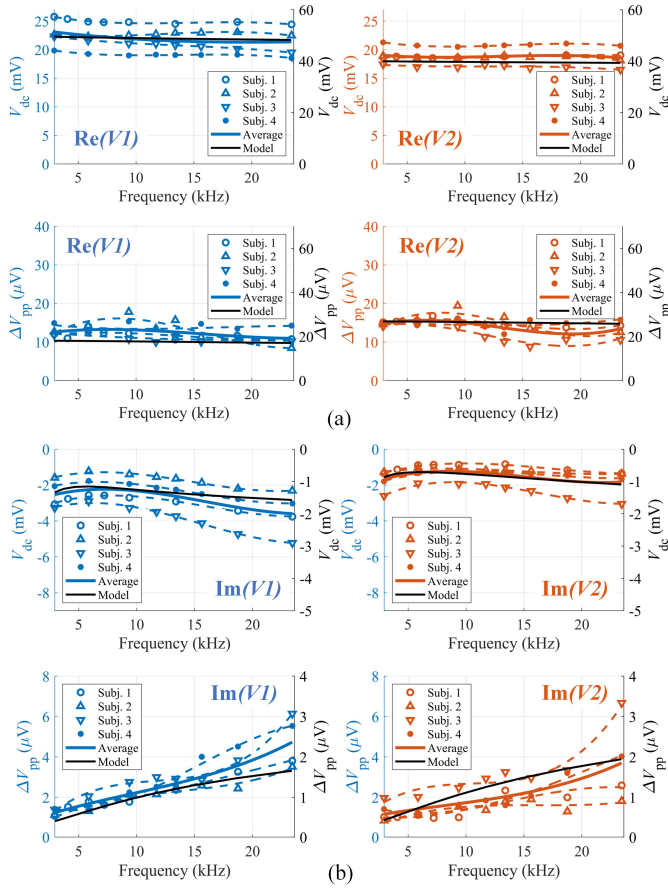


Fig. 19. The measurement and model results of  $V_{dc}$  and  $\Delta V_{pp}$  versus current injection frequency from 3 to 25 kHz for  $V1$  and  $V2$  (a) real part, (b) imaginary part.

measurements for each subject. The measured subjects' mean PTT decreased from 6.8 to 3.0 ms and the mean  $\Delta V_{pp}$  decreased from 40.6 to 25.4  $\mu\text{V}$  when  $X_d$  increased from 0 to 1.5 cm, in line with the simulation results. The proposed model showed the detailed behavior and explanation of PTT variation with sensing location, which helps in improving the estimation algorithms of hemodynamic parameters.

### E. Effect of the Current Frequency

We performed a Bio-Z frequency analysis by changing the frequency of the current injection from 3 to 25 kHz and monitoring the effect on  $V_{dc}$  and  $\Delta V_{pp}$  in simulation and measurements with electrode configuration like the PTT experiment in Fig. 18 with electrodes placed over the radial artery. Fig. 19 shows  $V_{dc}$  of the real and imaginary components of  $V1$  (i.e.  $\text{Re}(V1)$  and  $\text{Im}(V1)$ ) and  $V2$  (i.e.  $\text{Re}(V2)$  and  $\text{Im}(V2)$ ) versus frequency from 3 to 25 kHz. The measurements were done on 4 subjects by taking the average over 3 minutes of data collected at each frequency point at the radial artery. The measurements show that the  $V_{dc}$  and  $\Delta V_{pp}$  of the real component are around 20 mV and 15  $\mu\text{V}$ , respectively, which are much higher than the imaginary component with an average of 3 mV and 3  $\mu\text{V}$ . There is a small change in the  $V_{dc}$  and  $\Delta V_{pp}$  of the real component versus frequency. However,  $V_{dc}$  and  $\Delta V_{pp}$  showed an increase with frequency for the imaginary component. As shown before, the  $V_{dc}$  is higher for  $V1$  while  $\Delta V_{pp}$  is higher for  $V2$  which

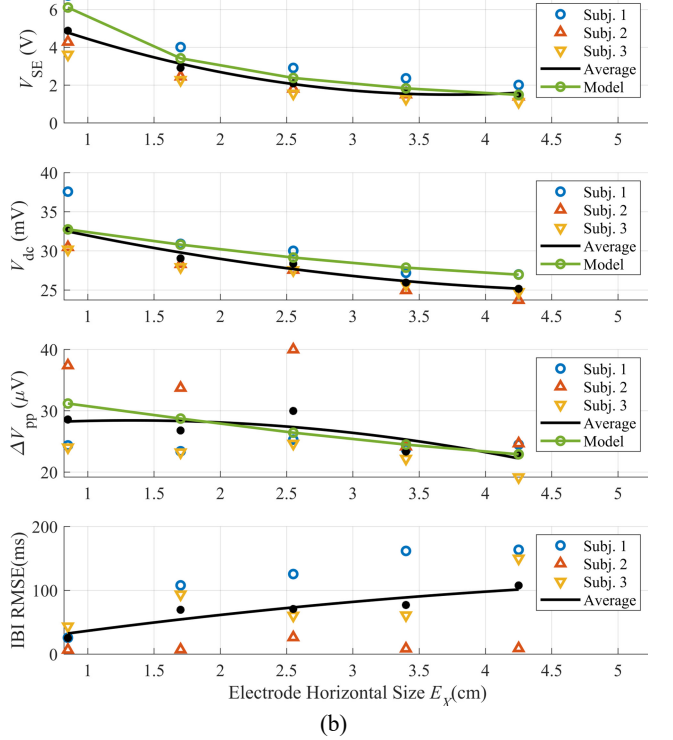
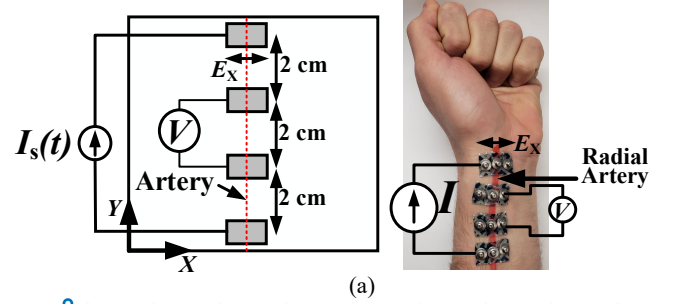


Fig. 20. Comparison between the simulated and measured  $V_{dc}$  and  $\Delta V_{pp}$  versus electrode horizontal size ( $E_x$ ).

is closer to the hand because of the smaller depth of the artery. These trends of the measurement results were successfully captured by the model results showing the dominance of the real part compared to the imaginary part for both  $V_{dc}$  and  $\Delta V_{pp}$ , which matches the components of the tissue impedance of fat, muscle, and blood.

### F. Effect of the Electrode Size

One of the most important design parameters in Bio-Z sensing is the size of the current and voltage electrodes. For wearable applications, it is preferable to minimize the electrode size to achieve a small-form factor. However, a smaller electrode results in a higher skin-electrode impedance, thus decreasing the injected current and signal-to-noise ratio for a fixed voltage supply of the current source. To our knowledge, the effect of the electrode size on the pulse amplitude and accuracy has not been studied before. In this subsection, we present the effect of changing the electrode size ( $E_x$ ) of the voltage and current electrodes from 0.85 to 4.25 cm on  $V_{dc}$  and  $\Delta V_{pp}$  while using a fixed current amplitude to understand the effect of changing only the electrode size. The results of the proposed simulation

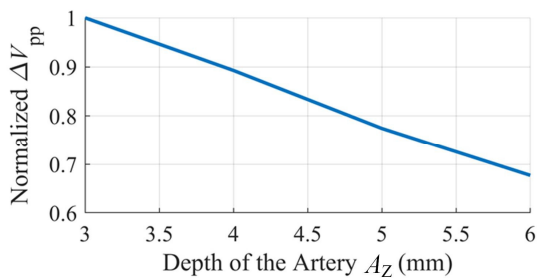


Fig. 21. Simulation results of  $\Delta V_{pp}$  versus artery's depth  $A_Z$ .

platform are compared with the measurements from 3 subjects.

To change the electrode horizontal size ( $E_X$ ), we used several small wet electrodes ( $E_X = 0.85$  cm,  $E_Y = 1.5$  cm) connected and stacked beside each other horizontally to provide variable  $E_X$  while keeping  $E_Y$  fixed, as shown in Fig. 20(a). The vertical spacing between electrodes was 2 cm. We used up to 5 electrodes stacked beside each other to change  $E_X$  from 0.85 to 4.25 cm in 5 steps centered at the radial artery. We started by adding one central electrode on the radial artery followed by data collection for 3 minutes while the hand was resting on the bench. Then the data collection was repeated by adding one electrode at a time on each side of the central electrode. The magnitude of the skin-electrode impedance was monitored after attaching each new electrode. The skin-electrode impedance decreased consistently with increasing  $E_X$ , as shown in Fig. 20(b). This was a verification step for the concept of stacking multiple electrodes beside each other to change  $E_X$ . Both simulations and measurements showed the decrease of average  $V_{dc}$  and  $\Delta V_{pp}$  with increasing  $E_X$ , as shown in Fig. 20(b). This is explained by the fact that Bio-Z is the measure of the impedance of a volume where its area is determined by the size of electrodes and its length is determined by the spacing between electrodes. Therefore, it is expected that  $V_{dc}$  will decrease as the electrode size increases due to a larger area of the measured volume. While  $\Delta V_{pp}$  decreased with  $E_X$  because the measured Bio-Z can be considered as the parallel equivalent of variable impedance due to blood flow and fixed impedance from the tissue. As the  $E_X$  increases, the fixed impedance increases while the variable impedance remains the same because it is a function of the size of the artery. Therefore, the weight of the variable part and  $\Delta V_{pp}$  decrease as the size of the electrode increases. In addition, the measured IBI RMSE relative to the reference PPG signal increases with  $E_X$  because of decreasing  $\Delta V_{pp}$ . We can conclude from these results that it is better to decrease the size of the electrode to be focused on the artery and get a larger and more accurate amplitude of pulse signal with a lower IBI error.

### G. Effect of the Artery's Depth

The artery's depth,  $A_Z$ , increases for individuals with high body mass index (BMI) because of a thicker fat layer under the skin. Increased  $A_Z$  results in lower pulse amplitude signal and lower quality of the estimations of the hemodynamic parameters. It is important to understand the effect of  $A_Z$  on the measured pulse signal to ensure reliable and robust sensing methods for all people with different BMI. However, it is difficult to characterize the effect of the artery's depth in the lab

and having simulations tools such as the proposed simulation platform that can provide accurate and quick results is very useful. We used the proposed model to quantify the depth of penetration of the Bio-Z signal into the tissue to reach the artery.  $\Delta V_{pp}$  at the surface was measured while changing the artery's depth  $A_Z$  from the average depth of 3 to 6 mm. The simulation results showed that the normalized  $\Delta V_{pp}$  decreased by only 32% when the artery's depth was doubled, as shown in Fig. 21. This demonstrates that Bio-Z is also suitable to detect pressure pulse waveform and hemodynamic parameters for individuals with high BMI.

## V. CONCLUSION

In this paper, we proposed a Bio-Z simulation platform using a 3D grid of the time-varying impedance voxels to model the tissue and pulse wave in the arteries by simulations in the SPICE environment in parallel with the sensing circuits. The proposed methods modeled the propagation of current through the small elements in the grid and the distribution of voltage at each node including the DC voltage of tissue and pulse signal from blood flow. The model was validated against Bio-Z measurements for the effect of different electrode locations relative to the artery, current frequency injection, and electrode size on the sensed pulse signal. The proposed method was used to quantify the penetration of the bio-impedance signals inside the tissue for different arterial depths. The proposed simulation platform can serve as an important tool to understand the propagation of pulse wave in the tissue and to improve Bio-Z sensing methods for measuring hemodynamic parameters and guide circuit designers and algorithm developers.

## REFERENCES

- [1] G. A. Mensah, G. A. Roth, and V. Fuster, "The Global Burden of Cardiovascular Diseases and Risk Factors: 2020 and Beyond," ed: Journal of the American College of Cardiology, 2019.
- [2] S. C. Smith *et al.*, "Our time: a call to save preventable death from cardiovascular disease (heart disease and stroke)," *Journal of the American College of Cardiology*, vol. 60, no. 22, pp. 2343-2348, 2012.
- [3] D. E. Bloom *et al.*, "The global economic burden of noncommunicable diseases," Program on the Global Demography of Aging, 2012.
- [4] E. Dolan *et al.*, "Superiority of ambulatory over clinic blood pressure measurement in predicting mortality: the Dublin outcome study," *Hypertension*, vol. 46, no. 1, pp. 156-161, 2005.
- [5] Y. L. Zheng *et al.*, "Unobtrusive sensing and wearable devices for health informatics," *IEEE Trans Biomed Eng.*, vol. 61, no. 5, pp. 1538-54, May 2014, doi: 10.1109/TBME.2014.2309951.
- [6] R. Mukkamala *et al.*, "Toward ubiquitous blood pressure monitoring via pulse transit time: theory and practice," *IEEE Transactions on Biomedical Engineering*, vol. 62, no. 8, pp. 1879-1901, 2015.
- [7] S. S. Thomas, V. Nathan, C. Zong, K. Soundarapandian, X. Shi, and R. Jafari, "BioWatch: A noninvasive wrist-based blood pressure monitor that incorporates training techniques for posture and subject variability," *IEEE journal of biomedical and health informatics*, vol. 20, no. 5, pp. 1291-1300, 2016.
- [8] C. Poon and Y. T. Zhang, "Cuff-less and noninvasive measurements of arterial blood pressure by pulse transit time," in *Engineering in Medicine and Biology Society, 2005. IEEE-EMBS 2005. 27th Annual International Conference of the*, 2006, pp. 5877-5880.
- [9] T. K. Bera, "Bioelectrical Impedance Methods for Noninvasive Health Monitoring: A Review," *J Med Eng*, vol. 2014, p. 381251, 2014, doi: 10.1155/2014/381251.

- [10] B. Ibrahim, D. A. Hall, and R. Jafari, "Bio-impedance spectroscopy (BIS) measurement system for wearable devices," in *Biomedical Circuits and Systems Conference (BioCAS), 2017 IEEE*, 2017: IEEE, pp. 1-4.
- [11] D. Dean, T. Ramanathan, D. Machado, and R. Sundararajan, "Electrical impedance spectroscopy study of biological tissues," *Journal of electrostatics*, vol. 66, no. 3-4, pp. 165-177, 2008.
- [12] B. Ibrahim, A. Akbari, and R. Jafari, "A novel method for pulse transit time estimation using wrist bio-impedance sensing based on a regression model," in *Biomedical Circuits and Systems Conference (BioCAS), 2017 IEEE*, 2017, pp. 1-4.
- [13] M.-C. Cho, J.-Y. Kim, and S. Cho, "A bio-impedance measurement system for portable monitoring of heart rate and pulse wave velocity using small body area," in *2009 IEEE International Symposium on Circuits and Systems*, 2009: IEEE, pp. 3106-3109.
- [14] B. Ibrahim and R. Jafari, "Cuffless Blood Pressure Monitoring from an Array of Wrist Bio-Impedance Sensors Using Subject-Specific Regression Models: Proof of Concept," *IEEE transactions on biomedical circuits and systems*, vol. 13, no. 6, pp. 1723-1735, 2019.
- [15] T. H. Huynh, R. Jafari, and W. Y. Chung, "An Accurate Bioimpedance Measurement System for Blood Pressure Monitoring," *Sensors (Basel, Switzerland)*, vol. 18, no. 7, 2018.
- [16] B. Ibrahim, D. A. Hall, and R. Jafari. "BioZPulse Simulation Platform." <http://www.github.com/TAMU-ESP/BioZPulse-Sim-Platform> (accessed 2019).
- [17] B. Ibrahim, D. A. Hall, and R. Jafari, "Bio-impedance Simulation Platform using 3D Time-Varying Impedance Grid for Arterial Pulse Wave Modeling," in *2019 IEEE Biomedical Circuits and Systems Conference (BioCAS)*, 2019: IEEE, pp. 1-4.
- [18] P. Avci et al., "Low-level laser (light) therapy (LLLT) in skin: stimulating, healing, restoring," in *Seminars in cutaneous medicine and surgery*, 2013, vol. 32, no. 1: NIH Public Access, p. 41.
- [19] J. Olsen, J. Holmes, and G. B. Jemec, "Advances in optical coherence tomography in dermatology—a review," *Journal of biomedical optics*, vol. 23, no. 4, p. 040901, 2018.
- [20] K. Sel, B. Ibrahim, and R. Jafari, "ImpediBands: Body Coupled Bio-Impedance Patches for Physiological Sensing Proof of Concept," *IEEE Transactions on Biomedical Circuits and Systems*, 2020.
- [21] M. Ring, C. Lohmueller, M. Rauh, and B. M. Eskofier, "A Two-Stage Regression Using Bioimpedance and Temperature for Hydration Assessment During Sports," in *2014 22nd International Conference on Pattern Recognition*, 2014: IEEE, pp. 4519-4524.
- [22] B. Ibrahim, D. Mrugala, and R. Jafari, "Effects of Bio-Impedance Sensor Placement Relative to the Arterial Sites for Capturing Hemodynamic Parameters," in *2019 41st Annual International Conference of the IEEE Engineering in Medicine and Biology Society (EMBC)*, 2019: IEEE, pp. 6569-6573.
- [23] W. Wang, M. Tang, M. McCormick, and X. Dong, "Preliminary results from an EIT breast imaging simulation system," *Physiological Measurement*, vol. 22, pp. 39-48, 2001, doi: 10.1088/0967-3334/22/1/306.
- [24] A. Tizzard, L. Horesh, R. J. Yerworth, D. S. Holder, and R. H. Bayford, "Generating accurate finite element meshes for the forward model of the human head in EIT," *Physiological Measurement*, vol. 26, no. 2, pp. S251-S261, 2005/03/30 2005, doi: 10.1088/0967-3334/26/2/024.
- [25] P. Kauppinen, J. Hyttinen, and J. Malmivuo, "Sensitivity Distribution Simulations of Impedance Tomography Electrode Combinations," *International Journal of Bioelectromagnetism*, vol. 7, pp. 344-347, 2005.
- [26] R. Abdelbaset, M. El Dosoky, and M. T. El-Wakad, "The effect of heart pulsatile on the measurement of artery bioimpedance," *Journal of Electrical Bioimpedance*, vol. 8, no. 1, pp. 101-106, 2019.
- [27] O. P. Gandhi, J. F. Deford, and H. Kanai, "Impedance Method for Calculation of Power Deposition Patterns in Magnetically Induced Hyperthermia," *IEEE Transactions on Biomedical Engineering*, vol. BME-31, no. 10, pp. 644-651, 1984.
- [28] M. Eberdt, P. K. Brown, and G. Lazzi, "Two-Dimensional SPICE-Linked Multiresolution Impedance Method for Low-Frequency Electromagnetic Interactions," *IEEE Transactions on Biomedical Engineering*, vol. 50, pp. 881-889, 2003, doi: 10.1109/TBME.2003.813534.
- [29] C. Dimas, N. Uzunoglu, and P. P. Sotiriadis, "A Parametric EIT System Spice Simulation with Phantom Equivalent Circuits," *Technologies*, vol. 8, no. 1, p. 13, 2020.
- [30] M. Kejarwal, K. Kaster, J. Jurist, and J. Pakanati, "Breast cancer detection using electrical impedance tomography: spice simulation," presented at the Proceedings of the Annual Conference on Engineering in Medicine and Biology, 1993.
- [31] A. Morimoto, E. Yasuno, Y. Kinouchi, Y. Ohmine, A. Tangoku, and T. Morimoto, "Spatial resolution in the electrical impedance tomography for the local tissue," in *2005 IEEE Engineering in Medicine and Biology 27th Annual Conference*, 2006: IEEE, pp. 6638-6641.
- [32] T. Dai and A. Adler, "Blood impedance characterization from pulsatile measurements," presented at the Canadian Conference on Electrical and Computer Engineering, 2006.
- [33] J. R. Matthie, "Bioimpedance measurements of human body composition: critical analysis and outlook," *Expert review of medical devices*, vol. 5, no. 2, pp. 239-261, 2008.
- [34] Y. M. Chi, T.-P. Jung, and G. Cauwenberghs, "Dry-contact and noncontact biopotential electrodes: Methodological review," *IEEE reviews in biomedical engineering*, vol. 3, pp. 106-119, 2010.
- [35] J. U. Kim, Y. J. Lee, J. Lee, and J. Y. Kim, "Differences in the properties of the radial artery between Cun, Guan, Chi, and nearby segments using ultrasonographic imaging: a pilot study on arterial depth, diameter, and blood flow," *Evidence-Based Complementary and Alternative Medicine*, vol. 2015, 2015.
- [36] S. Gabriel, R. Lau, and C. Gabriel, "The dielectric properties of biological tissues: III. Parametric models for the dielectric spectrum of tissues," *Physics in medicine & biology*, vol. 41, no. 11, p. 2271, 1996.
- [37] A. Tonks, J. Lawrence, and M. Lovie, "Comparison of ulnar and radial arterial blood-flow at the wrist," *The Journal of Hand Surgery: British & European Volume*, vol. 20, no. 2, pp. 240-242, 1995.
- [38] "Medical electrical equipment, Part 1: General requirements for basic safety and essential performance, ANSI/AAMI ES60601-1:2005/A1:2012," in "ANSI/AAMI ES60601-1:2005/A1:2012," ANSI/AAMI ES60601-1:2005/A1:2012, ANSI/AAMI ES60601-1:2005/A1:2012.



**Bassem Ibrahim** (S'12) is a Ph.D. candidate in Computer Engineering at Texas A&M University. He received his B.Sc. and M.Sc. degrees in Electrical Engineering from Ain Shams University, Cairo, Egypt in 2004 and 2012 respectively. His research interests include exploring new modalities for wearable physiological sensing as well as investigating machine learning and signal processing techniques to predict actionable information from physiological time-series data. He has 10 years of experience in the design of integrated circuits for sensors chips. He received the best poster award at BioCAS 2019.



**Drew A. Hall** (S'07–M'12–SM'19) received the B.S. degree in computer engineering with honors from the University of Nevada, Las Vegas, NV, USA, in 2005, and the M.S. and Ph.D. degrees in electrical engineering from Stanford University, Stanford, CA, USA, in 2008 and 2012, respectively. From 2011 to 2013, he was a Research Scientist in the Integrated Biosensors Laboratory at Intel Corporation, Santa Clara, CA, USA. Since 2013, he has been with the Department of

Electrical and Computer Engineering, University of California at San Diego, where he is currently an Associate Professor. His research interests include bioelectronics, biosensors, analog circuit design, medical electronics, and sensor interfaces. Dr. Hall won First Place in the Inaugural International IEEE Change the World Competition and First Place in the BME-IDEA invention competition, both in 2009. He received the Analog Devices Outstanding Designer Award in 2011, an Undergraduate Teaching Award in 2014, the Hellman Fellowship Award in 2014, an NSF CAREER Award in 2015, and an NIH Trailblazer Award in 2019. He is also a Tau Beta Pi Fellow. He has served as an Associate Editor of the IEEE TRANSACTIONS ON BIOMEDICAL INTEGRATED CIRCUITS since 2015, a member of the CICC Technical Program Committee since 2017, and a member of the ISSCC Technical Program Committee since 2020.



**Roozbeh Jafari** (SM'12) is the Tim and Amy Leach Professor of Biomedical Engineering, Computer Science and Engineering and Electrical and Computer Engineering at Texas A&M University. He received his Ph.D. in Computer Science from UCLA and completed a postdoctoral fellowship at UC-Berkeley. His research interest lies in the area of wearable computer design and signal processing with an emphasis on digital and mobile health. He has raised more than \$87M for

research with \$28M directed towards his lab. His research has been funded by the NSF, NIH, DoD (TATRC), AFRL, AFOSR, DARPA, DTRA, DIU, SRC and industry (Royal Philips, Texas Instruments, Tektronix, Samsung & Telecom Italia). He has published over 180 papers in refereed journals and conferences. He has served as the general chair and technical program committee chair for several flagship conferences in the area of Wearable Computers. Dr. Jafari is the recipient of the NSF CAREER award (2012), IEEE

Real-Time & Embedded Technology & Applications Symposium best paper award (2011), Andrew P. Sage best transactions paper award (2014), ACM Transactions on Embedded Computing Systems best paper award (2019), and the outstanding engineering contribution award from the College of Engineering at Texas A&M (2019). He has been named Texas A&M Presidential Fellow (2019). He serves on the editorial board for the IEEE Transactions on Biomedical Circuits and Systems, IEEE Sensors Journal, IEEE Internet of Things Journal, IEEE Journal of Biomedical and Health Informatics, IEEE Open Journal of Engineering in Medicine and Biology and ACM Transactions on Computing for Healthcare. He serves on scientific panels for funding agencies frequently, serves as a standing member of the NIH Biomedical Computing and Health Informatics (BCHI) study section (2017-2021), and as the chair of the NIH Clinical Informatics and Digital Health (CIDH) study section (2020-2021).